Scale-up of BiVO4 photoanode for water splitting in a photoelectrochemical cell : issues and challenges

Yao, Xin; Wang, Danping; Zhao, Xin; Ma, Susu; Bassi, Prince Saurabh; Yang, Guang; Chen, Wei; Chen, Zhong; Sritharan, Thirumany

2018

Yao, X., Wang, D., Zhao, X., Ma, S., Bassi, P. S., Yang, G., . . . Sritharan, T. (2018). Scale-up of BiVO4 photoanode for water splitting in a photoelectrochemical cell : issues and challenges. Energy Technology, 6(1), 100-109. doi:10.1002/ente.201700619

https://hdl.handle.net/10356/85907

https://doi.org/10.1002/ente.201700619

SCALE-UP OF $BiVO_4$ PHOTOANODE FOR WATER SPLITTING IN A PHOTOELECTROCHEMICAL CELL: ISSUES AND CHALLENGES.

*Xin Yao[+], Danping Wang[+], Xin Zhao, Susu Ma, Prince Saurabh Bassi, Guang Yang, Wei Chen, Zhong Chen, and Thirumany Sritharan**

School of Materials Science and Engineering, Nanyang Technological University, 50 Nanyang Avenue, 639798 Singapore, and
Singapore-Berkeley Research Initiative for Sustainable Energy (SinBeRISE), CREATE Tower, 1 Create Way, #11-00, 138602 Singapore.

Published in Energy Technology, Volume 6 (1), January 2018, pp 100 – 109.
DOI: 10.1002/ente.201700619

Keywords: photoanode, scale-up

Abstract: The monoclinic scheelite $BiVO_4$ is recognized as one of the promising candidate material for a photoanode because of its 9.1% theoretical efficiency for half-cell solar to hydrogen conversion. While significant research effort has been devoted to improving the PEC performance of this material, they have mainly been in small anode areas with only a handful of studies on scaled-up sizes. Herein, a facile metal-organic decomposition synthesis method was used to produce scaled-up Mo-doped $BiVO_4$ photoanodes. Multiple modifications were explored and incorporated to enhance the performance of the photoanode. A large area 5 cm × 5 cm photoanode was successfully prepared with all the modifications. The resulting photoanode gave a photocurrent density of 2.2 mA cm^{-2} at 1.23 V vs. RHE, under AM 1.5G illumination in a photoelectrochemical cell initially, and remained at 79% of this value after 1 h of operation. A deleterious effect of the increased anode surface area on the photocurrent density was observed which we term the "areal effect". Understanding the reasons for the areal effect is indispensable for the development of large scale PEC devices for water splitting.

[+]These authors contributed equally to this work.
*Corresponding author's e-mail: assritharan@ntu.edu.sg

Introduction

Solar hydrogen generation has the potential to be a sustainable energy source as the hydrogen could be used directly as a fuel, or could be used to reduce CO_2 to form hydrocarbon or oxyhydrocarbon fuels. A conventional electrochemical cell driven by solar panels could be used to split water and produce oxygen and hydrogen, but the energy losses in this technique need to be minimized. This could be achieved by decreasing the charge transportation distance scale to less than a millimetre, from a metre or higher scales. The oxygen evolution reaction (OER) has a higher energy barrier than the hydrogen evolution reaction (HER) and hence its catalysis is beneficial. Different avenues are being investigated for catalyzing the OER reaction at the anode such as, a catalyst activated by the current itself (electrocatalyst) or one that is activated by photons (photocatalyst). The conventional configuration of a photoelectrochemical cell (PEC) is well suited for experimenting with photoactive materials in the anode to promote the OER, and hence has been used as the vehicle by researchers considerably.[1] Many candidate photoactive semiconductor materials such as Fe_2O_3, WO_3 and $BiViO_4$ have been investigated, of which the monoclinic scheelite form of $BiVO_4$ has shown considerable promise as a photoanode material[2, 3] ascribed to its remarkable theoretical efficiency of 9.1% of half-cell solar to hydrogen conversion.[4, 5] This n-type $BiVO_4$ meets many requirements to be an efficient photoanode material, but it has some deficiencies too. This material is among the limited group of materials that absorb visible light effectively and is semiconducting. It also has energetically favorable band positions for charge carrier collection. Its valence band (VB) edge at ca. 2.4 V vs. reversible hydrogen electrode (RHE) provides sufficient overpotential for OER, while the conduction band (CB) edge is just below the thermodynamic level for H_2.[6] Its elements are cheap and earth-abundant, which are favorable attributes for large scale industrial application. On the other hand,

its deficiencies are intense carrier localization leading to significant recombination of photogenerated electron-hole pairs,[7] poor carrier mobility,[8] retarded kinetics of oxygen evolution,[9] insufficient photon absorption, and chemical and photoelectrochemical instability. In spite of its high theoretical capability, the efficiencies achieved in practice in pristine $BiVO_4$ photoanodes are typically less than 2%, in terms of half-cell solar to hydrogen conversion.[10] Various schemes have been attempted to circumvent one or more of the specific deficiencies of this material, and unlock its potential for PEC application. Methods such as doping, nanostructuring, band alignment, use of co-catalyst and so forth have been investigated.[8, 11] For example, doping by metal ions was investigated to change the intrinsic electrical and optical properties of $BiVO_4$,[12] introducing OER catalyst was targeted at boosting the water-splitting kinetics.[13]

It is noteworthy that the current stage state-of-the-art performance reports of $BiVO_4$ photoanodes were obtained in small areas of anodes, typically of the order of 2 cm^2 on FTO glass.[12, 14, 15] Scaling up the anode area to significant sizes, and achieving the reported performance in a repeatable manner is a formidable challenge. This is crucial to prove its viability at industrial scales. Such studies could become the focus for this application of $BiVO_4$ in future. Scaling up the $BiVO_4$ photoanode area from 2 cm^2 to about 20 cm^2 demands better control of the fabrication process to achieve film thickness and structure uniformity, and a good understanding of the mass transport of ions in the electrolyte. Besides, the performance of photoanodes could potentially be affected by certain unexpected factors, which in turn may require adaptations to the electrode, or the cell itself. For example, Hernández et. al reported that the electrode showed a decrease of photo-response when the photoactive area was enlarged.[16, 17] The authors attributed this detrimental

effect of increased area to the non-uniformity of photoactive film thickness. Stability and reliability of the anode in the cell environment is another major engineering requirement that must be met for commercial use of this technology.[18, 19]

In this work, we adapted a facile, metal-organic decomposition technique to fabricate large-scale, porous, $BiVO_4$ thin film electrodes of effective area 25 cm^2, on FTO substrates. To maximize the PEC performance of our photoanodes, the electronic properties of $BiVO_4$ were modified through n-type doping. For improvement of its charge carrier collection, provision of a WO_3 underlayer and a Co-Pi toplayer were found to be beneficial. Their fabrication was optimized to give the best performance through experimental trials. Scalable processes were used for fabrication of all layers. The photocurrent density of the optimized 25 cm^2 electrode reached 2.2 mA cm^{-2} at the onset of PEC water splitting operation with 1 Sun illumination and with a Pt cathode. It remained at 80% of this value even after 1 h of continuous operation. We continued to use this 25 cm^2 thin film $BiVO_4$ photoanode as a platform to investigate the general mechanism of degradation in the cell, during operation, which has an adverse effect on its performance.

Results

In our effort to fabricate large area thin film $BiVO_4$ photoanodes, facile controllability of the process was one of our primary aims along with achieving uniformity of thickness and structure in the film. Therefore we selected a metal-organic decomposition (MOD) technique as the synthesis scheme, because it is effective and could be scaled up to fabricate uniform films on large areas of FTO substrates with variable transparency, as shown in Figure S1.[20] Once the large area anode fabrication process was established, we examined three modifications to the pure $BiVO_4$ anode to enhance its photoelectrochemical properties. Our strategy was to evaluate the effects of

the modifications on the photocatalytic performance of $BiVO_4$, one at a time, and then combine multiple modifications, to finally arrive at a high-performance composite anode on a 5 cm × 5 cm FTO substrate.

FTO glass is the preferred transparent conducting electrode for PEC and solar cells because of its good electrical conductivity and optical transparency (even after calcination above 500 ℃). The conductivity of FTO glass is usually 2 to 3 times better than ITO (indium tin oxide) glass, and its mechanical strength is sufficient to endure the manufacturing steps employed in producing the anode and its assembly in PEC. In recent Artiphyction prototype,[17, 21] one hundred FTO pieces of size 8 cm × 8 cm were assembled to fabricate an anode of area 1.6 m^2 in a PEC cell for direct solar water splitting. This was possibly to simulate an industrial scale deployment. In academic research however, photoanodes used had typically less than 3 cm^2 photoactive areas. Hence, our aim of 5 cm × 5 cm anode area could be considered a pilot scale investigation, approaching the 8 cm × 8 cm pieces used to produce an industrial scale PEC anode. It could be reasonable to call photoelectrodes bigger than 25 cm^2 as large pieces, since this dimension is sufficient for making m^2 scale anodes by assembly.

MOD synthesis is readily amenable to nanostructuring of the $BiVO_4$ texture, which could contribute to enhanced charge separation of the photogenerated holes in a solid-liquid bulk heterojunction.[22] The n-type doping with a high valence metal ion (such as Mo and W) could also be simultaneously achieved in this synthesis method. In a previous study, doping with 3 at% Mo was found to increase the photocurrent density in a small area anode, and hence we choose to continue to expand on this finding.[20, 23] The thickness of the Mo-doped $BiVO_4$ (Mo- $BiVO_4$) film

was not previously optimized and hence we examined four levels of thickness from 50 to 230 nm. An un-doped $BiVO_4$ film of thickness 100 nm was also included in the test for comparison. Figure 1a shows the photocurrent density obtained for different applied electrode potentials. Firstly, this figure demonstrates that 3 at% Mo doping boosts the photocurrent density of $BiVO_4$ by up to 4 times compared to pure $BiVO_4$. Such remarkable increment could be attributed to an increased electrical conductivity, which facilitates the separation of photogenerated charges without significantly affecting the band gap.[24, 25] Also, as shown in Figure 1a, we demonstrated the effect of thickness on the performance of Mo-$BiVO_4$ film. Four thicknesses (50, 100, 160, 230 nm, details shown in Figure S2-S6) were examined and their linear-sweep voltammagrams (LSV) under front illumination of AM 1.5G solar simulator are compiled in Figure 1a. It is clearly shown that the 100 nm Mo-$BiVO_4$ film achieved considerably higher photocurrent density at 1.23 V although, the 160 nm thick film performed better at the high voltage range. In consequence, for all subsequent developments we used 100 nm thick Mo-$BiVO_4$ film as the basic anode.

To enhance the charge separation and collection, it would be beneficial to use an electron transport layer below the Mo-$BiVO_4$ film to prevent holes from entering the FTO and causing recombination. Among the electron transport compounds WO_3 is a good candidate because its calculated conduction band (CB) position is 3.0 eV vs. RHE, which is higher than the CB position of $BiVO_4$ (2.4 eV vs. RHE), while its valence band (VB) position of 0.5 eV vs. RHE is also more positive than that of $BiVO_4$ (0.1-0.3 eV vs. RHE).[26, 27] Hence, WO_3 could be an efficient underlayer to form a heterojunction with $BiVO_4$.[28, 29] Such heterojunction band alignment will enhance the transportation of electrons from the CB of $BiVO_4$ to that of WO_3, which in turn will suppress the

chances of recombination of photogenerated electrons and holes. In effect, the WO_3 underlayer serves as a "hole mirror" to block hole transport to the FTO conductive layer.[30]

For coating WO_3 on FTO we used magnetron sputtering which is a commercially available process. Metallic W was magnetron sputtered on the FTO substrate and then calcined in static air to oxidize the W to WO_3 nanoparticles. By this method a uniform coating of WO_3 could be obtained on FTO glass (Figure S7) which serves as the underlayer for the subsequent deposition of Mo-$BiVO_4$ film by MOD. Figure 1b displays the typical current density vs potential (J-V) curves for the Mo-$BiVO_4$ anodes with and without WO_3 underlayer. Upon front illumination by AM 1.5G solar simulator, the bare Mo-$BiVO_4$ film of 100 nm thickness showed only a current density of around 0.34 mA cm^{-2} at 1.23 V which monotonically increased to 1.59 mA cm^{-2} at 2.0 V. After introducing the WO_3 underlayer to Mo-$BiVO_4$ film of the same thickness, a significant enhancement to photo response is evident. The photocurrent density was boosted to 1.69 mA cm^{-2} at 1.23 V vs. RHE and reached a peak of 2.8 mA cm^{-2} which clearly demonstrates the benefit of the underlayer. Three thickness levels of 25, 50 and 100 nm of WO_3 were examined (details shown in Figure S10-S12) to assess the thickness effect on the photocurrent. The three electrodes with the different WO_3 layer thicknesses demonstrated photo response current densities of 1.45, 1.59, and 1.24 mA cm^{-2} at 1.23 V, respectively. It is evident that the 50 nm thickness exhibits the best photo activity. Therefore, we choose a 50 nm thick WO_3 underlayer to enhance the performance of our 3 at% Mo doped $BiVO_4$ anodes.

As the final step of improvement, we addressed the issue of slow oxygen evolution kinetics of the Mo-$BiVO_4$-electrolyte interface.[13] A common solution to such issues is to use a co-catalyst at the

Mo-$BiVO_4$ surface to catalyse the OER. Various co-catalysts have been used by researchers among which the amorphous Co-Pi has been a popular choice to increase the OER efficiency for several photoanode materials such as Fe_2O_3,[31, 32] WO_3[33] and $BiVO_4$. [34, 35] Hence, Co-Pi is an obvious candidate material in our investigations also. Besides Co-Pi, we also evaluated other potential candidates such as $NiFeO_x$, TiO_x and TiO_2 (details elucidated in Figure S13-S15 of supporting information) but, they were found to be inferior to Co-Pi. Having dismissed the other materials by the screening experimentation, we went on to optimize the loading of Co-Pi using galvanostatic electrodeposition by controlling the electric charge (or conditioning time). The LSV in Figure 1c reflects the performance of five Mo-$BiVO_4$/CoPi samples with different Co-Pi loading. The figure indicates that the best photocurrent density of 1.58 mA cm^{-2} was achieved at 1.23 V, with the conditioning of 2.5 mC cm^{-2} for Co-Pi loading. The performance with Co-Pi at this loading was nearly 4 times higher in terms of photocurrent density, compared with the bare Mo-$BiVO_4$ sample.

After these three modifications, namely (i) 3 at% Mo doping of the $BiVO_4$, (ii) incorporation of a 50 nm WO_3 underlayer, (iii) application of a Co-Pi overlayer at optimum loading, PEC performance of our large-area composite anode did show improvement for each modification. It is envisaged that a combination of the three features will synergise into a much improved photoanode, comparable to other state-of-the-art $BiVO_4$-based nanomaterials. Figure 1d and Table 1 specifically depict the quantitative improvement in photocurrent density achieved in our nanostructured $BiVO_4$ at 1.23 V vs. RHE. They show the improvements achieved for each modification developed here in large area anodes. The Mo doping alone initially enhanced the current density from 90 μA cm^{-2} to 340 μA cm^{-2} which can be derived by comparing the curves

for pure $BiVO_4$ and the doped $BiVO_4$. Incorporating a 100 nm thick WO_3 underlayer to Mo-$BiVO_4$ then boosted the current density to 1.78 mA cm^{-2}. Application of an overlayer of amorphous Co-Pi to the Mo-$BiVO_4$ film, along with the underlayer finally increased the current density to a creditable 2.20 mA cm^{-2}.

It's not the first time that the $WO_3/BiVO_4$ heterojunction, combined with Co-Pi, was used for the photoanode of PEC.[36, 37] The MOD method for the synthesis of n-type doped $BiVO_4$ was also employed in previous studies.[20, 22] For example, Park et. al proposed the $WO_3/BiVO_4$/Co-Pi design and achieved a photocurrent density of 2.4 mA cm^{-2} on 1.5 cm x 3 cm FTO substrate (at 1.23V vs. RHE in a PH 7 phosphate electrolyte).[37] In their case, both $BiVO_4$ and WO_3 were spin coated and Co-Pi was electrochemically deposited. In another work of $WO_3/BiVO_4$/Co-Pi ternary photoanode reported by Joo et. al,[36] WO_3 nanorods were synthesized via hydrothermal method and were covered by spin coated $BiVO_4$ thin film, and then Co-Pi overlayer was electrochemically deposited. Their good structural control resulted in a photocurrent density of 3.3 mA cm^{-2} at 1.23 V vs. RHE. In our modified procedures, we adopted the direct drop casting for preparation of Mo-$BiVO_4$ thin film and magnetron sputtering for introducing WO_3. Both procedures are more time-saving and cost-effective, with the opportunity to achieve good uniformity of films. In order to show the competitiveness of our material, we have compared the PEC performance of some state-of-the-art $BiVO_4$ photoanodes from recent publications in Table S1. The best performance among them, in terms of photocurrent density, was reported by Domen et al. in a Ni/Sn supported $BiVO_4$ photoanode, enhanced with the self-generated NiFe catalyst. They achieved ~ 3.2 mA cm^{-2} photocurrent density at 0.4 V vs. RHE.[38] Although, the performance of our systematically developed photoanode is lower, it is a creditable development for large area anodes, achieved by

a combination of modifications enabled by versatile and commercially viable processes. It is an outcome balanced between large capacity and efficiency, with promise for large-scale application.

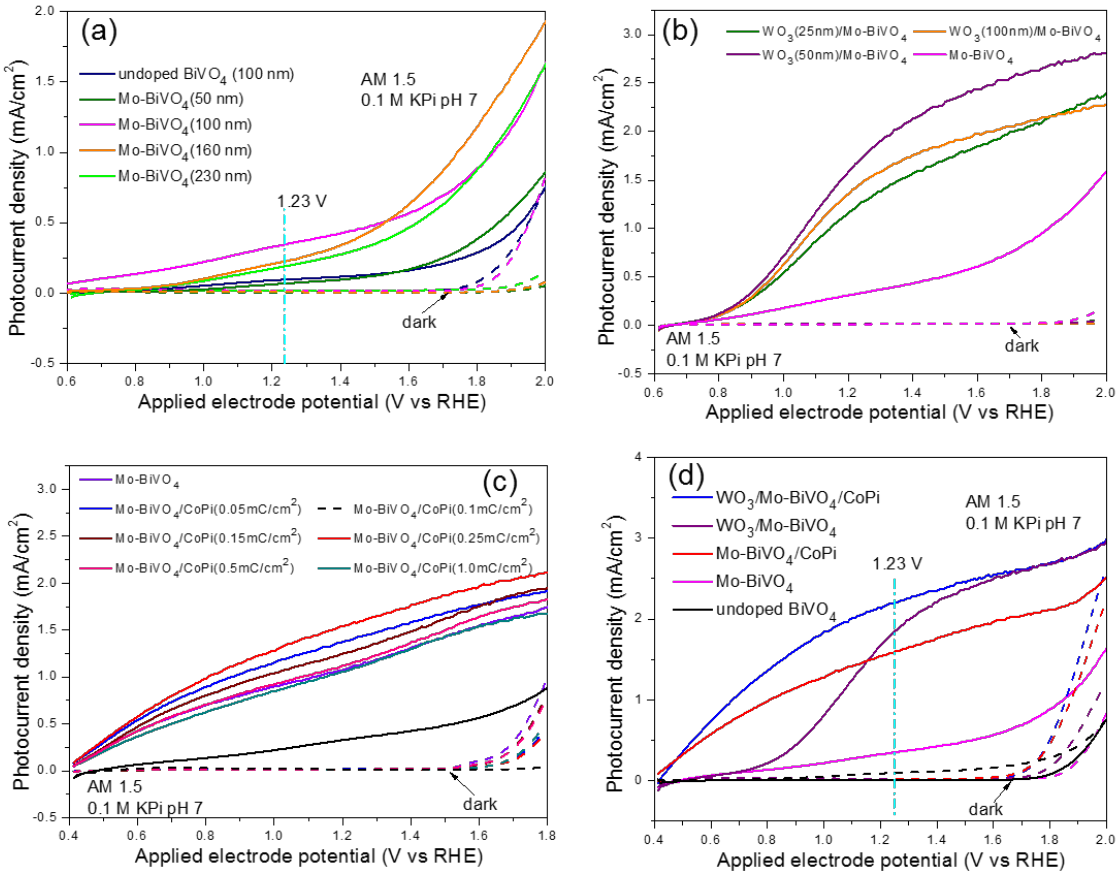

Figure 1. a) LSV scans of one undoped $BiVO_4$ (100 nm thick) and three Mo-$BiVO_4$ with different thicknesses of 50, 100, 160 and 230 nm in dark and under AM 1.5G illumination. b) LSV scans in dark and under AM 1.5G illumination for Mo-$BiVO_4$ and WO_3/Mo-$BiVO_4$ of different WO_3 thicknesses (25, 50 and 100 nm). c) LSV scans in dark and under AM 1.5G illumination for WO_3/Mo-$BiVO_4$/Co-Pi of different Co-Pi loading (0.05, 0.1, 0.15, 0.25, 0.5, 1.0 mC cm^{-2} for electrodeposition). d) LSV scans in dark and under AM 1.5G illumination for undoped $BiVO_4$, Mo-$BiVO_4$, WO_3/Mo-$BiVO_4$ and Mo-$BiVO_4$/Co-Pi and WO_3/Mo-$BiVO_4$/Co-Pi.

Table 1. The photocurrent densities of different photoanodes under AM 1.5G illumination, at 1.23 V vs. RHE.

Material	Photocurrent density (mA cm^{-2})
WO_3/Mo-$BiVO_4$/CoPi	2.20
WO_3/Mo-$BiVO_4$	1.78
Mo-$BiVO_4$/CoPi	1.58
Mo-$BiVO_4$	0.34
undoped $BiVO_4$	0.09

Figure 2a shows samples of the as-prepared photoanodes of size 5 cm × 5 cm consisting WO_3/Mo-$BiVO_4$/Co-Pi layers sequentially deposited on the FTO substrate and a similar anode of size 1 cm × 2 cm. The reflection, transmission, and absorption spectra obtained in the large area anode are shown in Figure 2b. The absorption edge of the sample is near 510 nm wavelength which corresponds to a band gap of 2.4 eV of $BiVO_4$. Each layer was characterized by x-ray diffraction (XRD) and electron microscopy after deposition. Their XRD data is given in Figure 2c where the crystal structures of WO_3 and $BiVO_4$ (monoclinic JSPDF: #01-75-1867) could be confirmed. A hump appears in the range 20-40° in the XRD patterns which is present even in the FTO glass. This could be attributed to the amorphous glass.[39] The Co-Pi being amorphous was not detected by XRD. It is important to note that traces of any crystalline impurities were not detected by XRD.

The scanning electron microscopy (SEM) of the cross-section of the optimized anode sample is shown in Figure 3a. Two distinct planar layers of WO_3 and $BiVO_4$ can be clearly distinguished above the FTO, with respective approximate thicknesses of 50 and 100 nm. The top view of WO_3 (Figure S7-S9) indicate the layer to be dense and coarse with numerous nanoparticles but it covers

the FTO substrate quite evenly. Unexpectedly, we found that the WO_3 coated FTO exhibited a beneficial improvement in wettability during the subsequent drop casting of the Mo-$BiVO_4$ organic precursors when compared to bare FTO.

In contrast to the WO_3 layer, the Mo-$BiVO_4$ layer was nanostructured with interconnecting "worm-like" branches leading to significant porosity, as evident in Figure 3b. The porosity level and thickness of the Mo-$BiVO_4$ film seem to be quite uniform over the area as indicated by the top and cross-sectional SEM images. A similar structure was reported in a previous study on Mo-$BiVO_4$ films and the authors then suggested that the high surface area arising from such a porous structure would shorten the diffusion lengths for photogenerated charge carriers. Consequently, this favors charge separation across the solid-liquid bulk heterojunction.[22] Figure 3c is a higher magnification image of the Mo-$BiVO_4$ film surface to show the amorphous Co-Pi nanoparticles (at 0.25 mC cm^{-2} loading) on the surface of the larger Mo-$BiVO_4$ grains. The Co-Pi nanoparticles appear to have weaved into a distinct mesh covering the whole surface of the Mo-$BiVO_4$ grains. However, it must be noted the Mo-$BiVO_4$ grains beneath the top surface that are visible in Figure 3c do not exhibit any Co-Pi particle coating. Hence, the Co-Pi deposition process appears not have penetrated the porosity of the Mo-$BiVO_4$ film to get to the deeper $BiVO_4$ grains in its porous structure. This may be attributed to poor contact of the interior grains with the solvent during the electrochemical conditioning process to deposit the Co-Pi probably due to the high surface energy of the aqueous electrolyte.[40] Overcoming this obstacle and achieving a complete coating of Co-Pi grains, well inside the porous network, perhaps by using a lower surface energy solvent, will be the next challenge in this project.

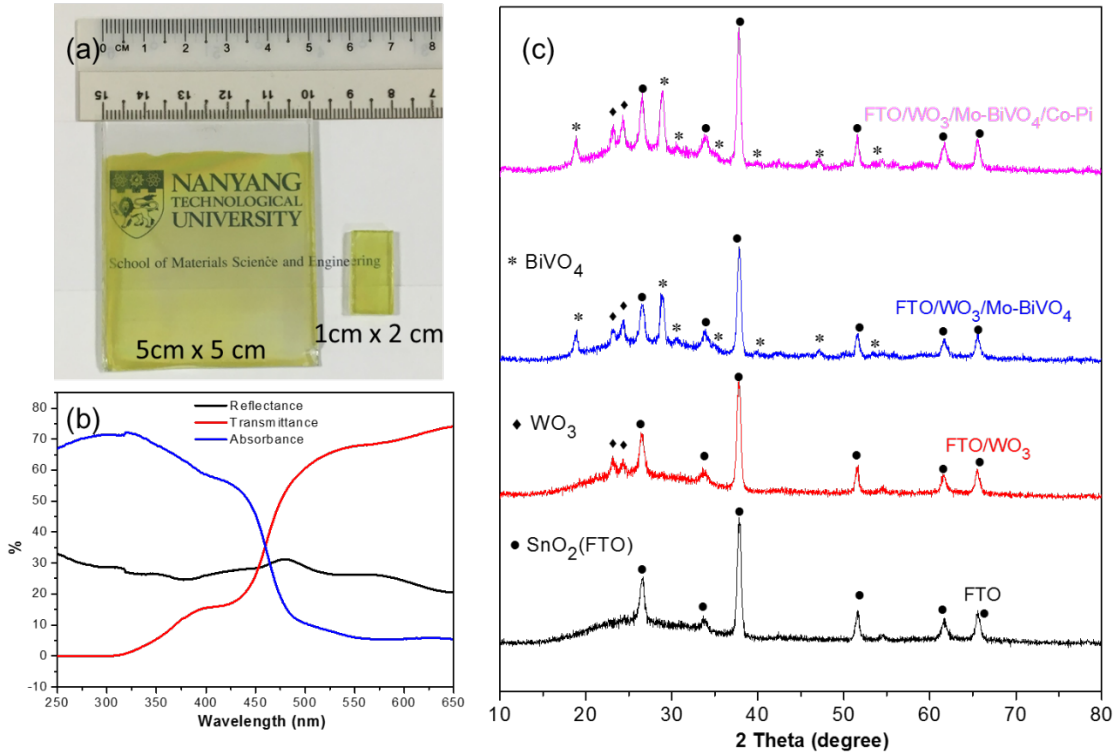

Figure 2. a) Optical images of the 5 cm × 5 cm and 1 cm × 2 cm samples of WO_3/Mo-$BiVO_4$/Co-Pi. b) Reflection, transmission and adsorption spectra of the WO_3/Mo-$BiVO_4$/Co-Pi sample. c) XRD patterns of FTO, FTO/WO_3, FTO/WO_3/Mo-$BiVO_4$, and FTO/WO_3/Mo-$BiVO_4$/Co-Pi

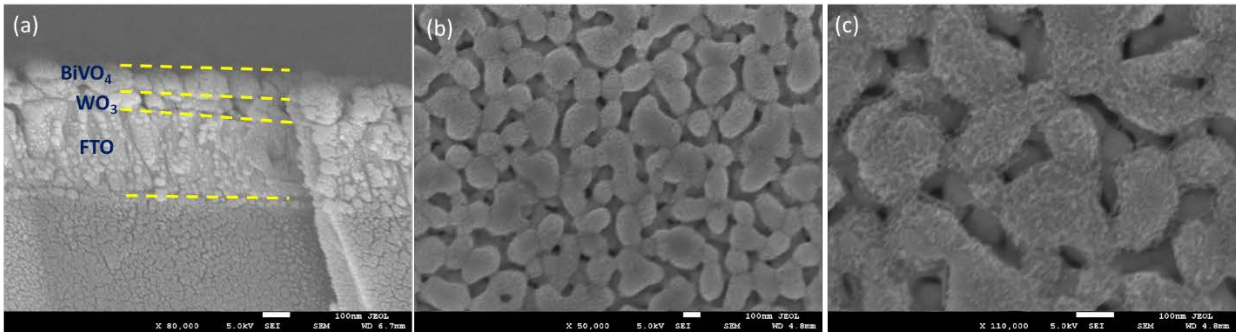

Figure 3. a) SEM images for the cross-sectional view of the WO_3/Mo-$BiVO_4$/Co-Pi product on FTO glass. b, c) Top-view SEM images of the porous WO_3/Mo-$BiVO_4$/Co-Pi photoanode.

Issues and challenges

1. Performance depreciation in scaled-up PEC

After a painstaking experimental program to enhance the performance of $BiVO_4$ photoanode in PEC, we implemented multiple processing steps to arrive at this composite thin film anode structure consisting WO_3/Mo-$BiVO_4$/Co-Pi layers on FTO. Now we proceed to discuss its performance in a scaled-up PEC cell that can take an anode of active area 5 cm × 5 cm. Figure 4a demonstrates our test bed setup that was used to investigate the photo response of the 5 cm × 5 cm photoanodes. This was designed and fabricated in-house. The cathode used was Pt wire gauze. Evaluation of the photo response of the large anodes proved that it is difficult to reproduce the high photocurrent densities obtained in the smaller scale anodes and PEC. The effective area of the anode appears to have a direct correlation with the photocurrent density even when all other water splitting conditions were same. We refer to this effect of anode area as the "areal effect". This is an adverse effect and we attribute it to the electrode/PEC dimensions. The scientific reasons for the areal effect are not clear but could be hypothetically attributed to increased charge recombination, electrical resistance, and ionic flux in the electrolyte. We found that the photocurrent density depreciates rapidly as the anode size is enlarged when all other factors are unchanged. We conducted two experiments to explicitly demonstrate the existence of the areal effect.

In the first experiment, two photoanodes of different effective areas, namely 1 cm × 2 cm and 5 cm × 5 cm, were produced consisting the newly developed multiple layers by the same processes. Figure 4b compares their LSV data where a severe depreciation in photocurrent density is apparent for the larger anode. The smaller anode showed a photocurrent density of 2.20 mA cm^{-2} at 1.23 V

vs. RHE and ended up with 2.99 mA cm^{-2} at 2.0 V. Meanwhile the larger one only reached 0.74 mA cm^{-2} and 1.05 mA cm^{-2} at 1.23 and 2.0 V respectively.

In the second experiment, a set of five masks were made, each having a circular aperture of area 0.125, 0.23, 0.5, 1, 2 cm^2 respectively at the center. Optical photos of these masks are shown in Figures S19 and S20. A 5 cm × 5 cm WO_3/Mo-$BiVO_4$ sample (without the Co-Pi) was used as the photoanode to split water in the PEC with an aqueous solution of 0.1 M KH_2PO_4 (KPi) as the electrolyte at PH 7. The masks were used to illuminate only the aperture areas and block the rest of the anode. By this, we were able to progressively increase the illumination area on the same large area anode, starting from 0.125 cm^2 to 2 cm^2, while all other conditions remained unchanged. This experiment will eliminate other possible variables that may be present when different anodes of different areas are used, as in the first experiment. The photocurrent obtained for each area of illumination is shown in Figure 4c where a decrease in current density with increase of illumination area is evident. The current densities at 1.23 V vs. RHE obtained from Figure 4c are 2.32, 2.08, 1.81, 1.58, 1.38 mA cm^{-2} for illumination areas 0.125, 0.23, 0.5, 1, 2 cm^2 respectively. This data is plotted in Figure 4d which shows a steady decrease of current density with increase of area. The photocurrent density for an illumination area of 0.125 cm^2 was 68% higher than that for 2 cm^2. Figure S21 shows the distribution of light intensity within the central circular area of diameter 2 cm in the light beam. It is clear from this measurement that the difference in light intensity between the center and the periphery is within 10 % which is much smaller than the decrease in photocurrent density attributed to the areal effect. Further investigations showed that this areal effect persisted even upon back illumination, and even in a different electrolyte, as exemplified in Figures S23, S24.

Since the area of illumination has a significant, deleterious effect on the photocurrent density, this could become a focus area of research in the future, and a bottleneck for large scale industrial effort. It is of paramount importance to understand the fundamental reasons for this areal effect in order to circumvent it. Based on our preliminary investigations, it is hypothesized that the increased electrical resistance of the FTO substrate, and the non-linear diffusion of reactants (namely OH^-) towards the electrodes could be two plausible causes for the areal effect. Since we are not able to quantify the areal effect on photocurrent density at present, it is prudent to record the illuminated area as an essential parameter when reporting photocurrent densities or efficiencies in water splitting using photo active electrodes.

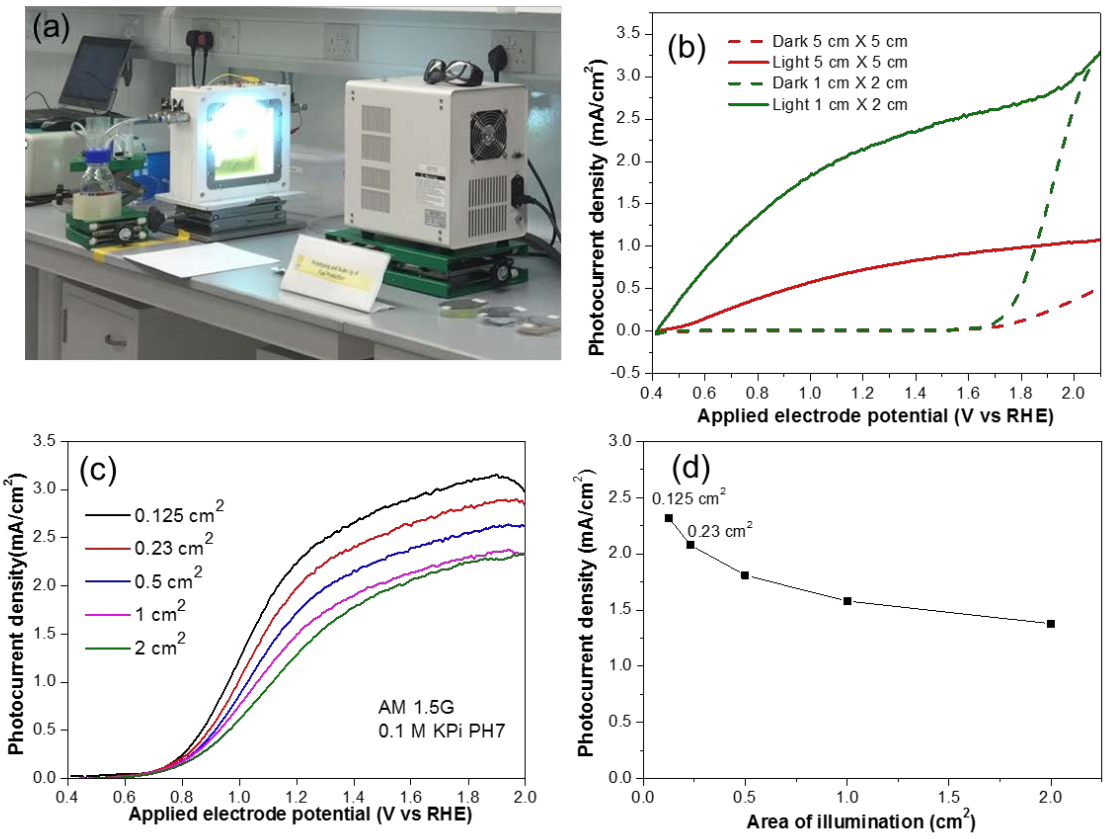

Figure 4. a) Photo of the large-scale PEC test bed setup. b) J-V curves of 1 cm × 2 cm and 5 cm × 5 cm WO_3/Mo-$BiVO_4$/Co-Pi photoanodes in dark and under AM 1.5G illumination. c) LSV scans of WO_3/Mo-$BiVO_4$ photoanode with controlled illuminated area of 0.125, 0.23, 0.5, 1 and 2 cm^2. To avoid interference from dark current, the J-V curves in this graph were already deducted by dark current. d) The calculated net photocurrent densities of WO_3/Mo-$BiVO_4$ photoanode in 0.1 M KPi electrolyte (PH 7) under AM 1.5G illumination, with different illuminated areas.

2. Instability of the anode

$BiVO_4$ is known to suffer from some chemical and photoelectrochemical instability, even in neutral pH condition. A recent modelling study implied that the accumulation of photogenerated charge carriers on the crystal surface could destabilize the lattice,[41] but the actual mechanism of photo corrosion in $BiVO_4$ is not fully understood yet. Attempts to protect the $BiVO_4$ from photo corrosion employed two techniques: 1) to coat an ultrathin layer of a corrosion-resistant oxide to isolate the $BiVO_4$ from of the electrolyte while allowing the photogenerated holes to tunnel through;[42, 43, 44] 2) to apply a stable OER catalyst on $BiVO_4$ to rapidly consume the holes and avoid the accumulation of charge carriers.[18, 45, 46] The Co-Pi overlayer used in this work could be classified as the latter technique. A comparison of the stability (the ratio of real-time photocurrent density to the initial photocurrent density) of three anodes is shown in Figure 5a. It is evident that deposition of the Co-Pi overlayer improves the stability of WO_3/Mo-$BiVO_4$ photoanode, which allows the devised photoanode to operate longer without significant loss of current output. During a 1 h stability test, 79% of initial photocurrent density was retained by the WO_3/Mo-$BiVO_4$/Co-Pi anode, which is 27% higher than the corresponding anode without Co-Pi. It is also noteworthy that the WO_3 underlayer also contributed to about 25% stability enhancement which is probably due to improved charge transfer which mitigates undesirable recombination or accumulation.

The long-term stability was examined by continuously operating the PEC with 5 cm × 5 cm WO_3/Mo-$BiVO_4$/Co-Pi anode for 13 h in 0.5 M Na_2SO_4 (PH 6) at 1.23 V. The decay of photocurrent density with time is shown in Figure 5b where the current density decays to1.24 mA cm^{-2} in 13 h which is about a half of the initial value. The aforementioned, incomplete coverage of Co-Pi on the $BiVO_4$ grains beneath the film surface could have contributed to this instability. In addition, pure $BiVO_4$ itself is supposedly more susceptible to photocorrosion than mainstream photocatalysts.[3] Stability appears to be the Achilles' heel of $BiVO_4$ at present. The stability observed in 0.1 M KPi solution (PH 7) was much worse than in 0.5 M Na_2SO_4 solution (PH 6) as evident from Figure S25. This is the reason for choosing 0.5 M Na_2SO_4 solution (PH 6) as the electrolyte above for stability assessment.

Lewis et al. designed a bi-layer thin film of TiO_2/Ni on $BiVO_4$,[19] to increase the stability of the photocatalyst in basic conditions. During a 2 h potentiostatic testing at 1.23 V vs. RHE in KOH electrolyte (PH 13), this surface passivated electrode demonstrated almost no depreciation of photocurrent density. However, the passivation layer didn't improve the OER efficiency, and the maximum photocurrent density obtained was around 1.4 mA cm^{-2} (at 1.23 V) which is insufficient compared with other photoanode materials. Recently, Choi et al. investigated a $ZnFe_2O_4$ layer to enhance the stability as well as photoelectrochemical performance of $BiVO_4$ in basic electrolyte.[47] The initial photocurrent density at 1.23 V vs. RHE was enhanced to 2.74 mA cm^{-2}, in KPi (PH 13) electrolyte, but it decreased to less than 2.0 mA cm^{-2} in less than 1 h. Domen et al. reported an impressive long-term stability of their CoO_x loaded $BiVO_4$ photoanode with ultrathin NiO layer[48] which showed only a little decay in performance over 16 h, but at relatively low applied bias of only 0.8 V vs. RHE. Compared with other semiconductors such as TiO_2, $BiVO_4$ is a more efficient

photon absorber but is more vulnerable for photocorrosion. A corrosion-resistant co-catalyst layer that can boost the photoelectrochemical reactivity and increase the stability of $BiVO_4$ photoanode simultaneously would unlock the full potential of this promising material.

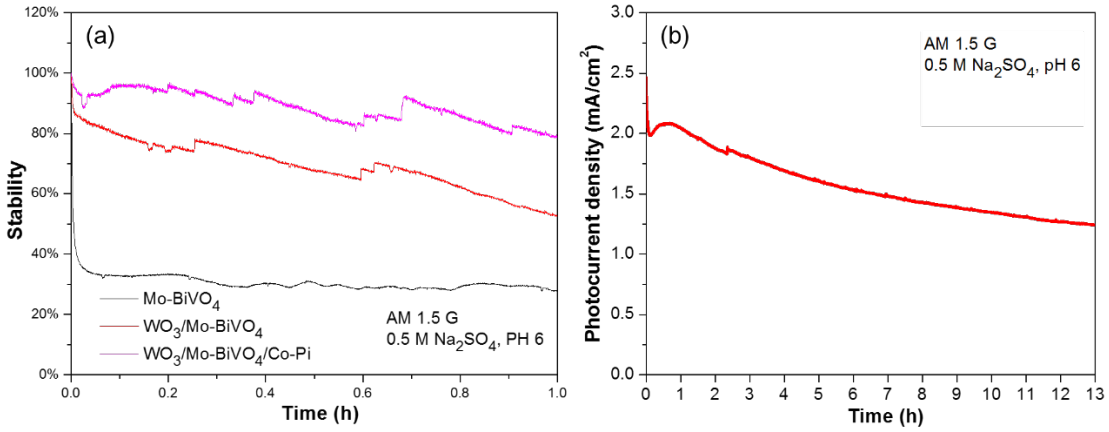

Figure 5. a) Stability-time curves of Mo-$BiVO_4$, WO_3/Mo-$BiVO_4$, and WO_3/Mo-$BiVO_4$/Co-Pi photoanodes under AM 1.5G illumination, in 0.5 M Na_2SO_4 solution (PH 6). b) Current-time curve of WO_3/Mo-$BiVO_4$/Co-Pi under 13 h of AM 1.5G illumination, in 0.5 M Na_2SO_4 solution.

Conclusions

In this work, we utilized a facile metal organic decomposition synthesis process to scale-up $BiVO_4$ thin film deposition on FTO and investigated its performance as a photoactive anode in a PEC with Pt cathode. We investigated and fine-tuned three modifications to this anode to enhance its performance which are: 1) a 100 nm thick film of 3 at% Mo doped $BiVO_4$, 2) a 50 nm WO_3 underlayer to block holes, 3) a Co-Pi overlayer as a co-catalyst to enhance the OER. The resulting anode consisted of a layered structure on FTO which could be denoted as WO_3/Mo-$BiVO_4$/Co-Pi. This optimized anode exhibited a photocurrent density of 2.2 mA cm^{-2} in 0.1 M KPi solution (PH

7) at 1.23 V vs. RHE. Whilst this being not the highest performance reported for $BiVO_4$-based anodes, the scalability and controllability of the fabrication processes, and the developed modifications are valuable for industrial requirements.

This newly developed photoanode exhibited 79% of the initial photocurrent density after 1 h of operation to split water in a PEC. It remained at 50% of initial current density after 13 h of operation. This indicates reasonable stability for the anode. In continuing studies, we aim to understand the prevailing photocorrosion mechanisms of Mo-$BiVO_4$, and devise protective measures accordingly to further enhance its stability.

An undeniable, deleterious areal effect was observed which diminished the photocurrent density as the active area of photoanode was increased. The actual reason for this areal effect is not understood yet but, electrical resistance of the FTO substrate and non-linear diffusion of reactant ions in the electrolyte could be contributors. Hence, we propose that researchers record the active anode area when reporting photocurrent densities or efficiencies in PEC water splitting studies.

Materials and Methods

Preparation of WO_3 underlayer: FTO glass was purchased from Latech Scientific Supply Pte. Ltd. (Singapore). The as-received FTO glass showed a sheet resistance of ~13.4 Ω, which slightly increased to ~14.4 Ω after 2 h calcination at 500 ℃. Thickness of FTO coating layer is around 400 nm. The transmittance of FTO glass is higher than 80%. A layer of metallic tungsten was first deposited on FTO (1 cm × 2 cm or 5 cm × 5 cm) by direct current (D.C.) magnetron sputtering, using a pure tungsten target and a plasma of argon as gas carrier. The sputtering chamber was first

pumped down to a gas pressure less than 1×10^{-5} mbar and then the sputtering was performed at 230 W for different durations. Immediately after the sputtering, the tungsten covered FTO was transferred to a muffle furnace and calcined in air at 500 ℃ for 2 h, with a ramping rate of 5 ℃ min^{-1}, to further convert metallic tungsten into tungsten oxide. The thicknesses of the resulting WO_3 layer depends on the sputtering duration. For WO_3 layers of 25, 50, 100 nm thicknesses, the corresponding sputtering times are 30, 60 and 120 s.

Preparation of WO_3/Mo-$BiVO_4$ Photoanode: A metal-organic decomposition method was employed for the preparation of porous Mo-$BiVO_4$ thin film on FTO/WO_3 substrate. Three precursors, $Bi(NO_3)_3 \cdot 5H_2O$ in glacial acetic acid (0.2 mol L^{-1}), vanadylacetyl acetonate in acetylacetone (0.03 mol L^{-1}) and molybdenyl acetylacetonate in acetylacetone (0.01 mol L^{-1}) were mixed according to the stoichiometric ratio of Bi : V : Mo = 100 : 97 : 3, and then diluted by different coefficients with acetylacetone. For the preparation of undoped $BiVO_4$, the Mo precursor was not added and the stoichiometric ratio of Bi : V was 1 : 1. The concentration of diluted solution determines the thickness of Mo-$BiVO_4$ thin film. For the Mo-$BiVO_4$ of 50, 100, 160, 230 nm thicknesses, the corresponding precursor mixtures were diluted by 6, 3, 2, 1.5 times. In the next step, a 0.75 ml of the diluted precursor solution was drop cast onto a piece of FTO/WO_3 (1 cm × 2 cm or 5 cm × 5 cm) on a 50 ℃ hotplate. The solvent mixture spread evenly on the surface of FTO/WO_3 because of the relatively low surface tension of acetylacetone. After drying, the glass was further heated in a furnace at 470 ℃, for 30 min followed by natural cooling down to room temperature.

Preparation of WO_3/Mo-$BiVO_4$/Co-Pi Photoanode: An electrochemical cell with three-electrode configuration was employed for the Co-Pi electrodeposition. The Pt foil was used as counter electrode and Ag/AgCl (in saturated KCl solution) was used as the reference electrode. 0.5 mM

$Co(NO_3)_2$ was added into 0.1 M KPi solution to serve as the electrolyte, and the pH was tuned to 7. For the electrodeposition, a constant current density of 0.006 mA cm^{-2} was applied to the WO_3/Mo-$BiVO_4$ sample, and the loading amount of Co-Pi was adjusted by the electrical charges (or deposition time). After the electrodeposition, the WO_3/Mo-$BiVO_4$/Co-Pi samples were cleaned in deionized water.

Characterization of Materials: Morphological characterization was conducted in field emission SEM (JSM-7600F, JOEL) and TEM (JEM 2010, JOEL). Crystallographic characterization was performed in thin film XRD (Shimadzu XRD-6000, Shimadzu) by applying Cu K_α radiation at 40 kV and 30 mA. The light absorption was evaluated by reflectance and transmission spectra, performed on a UV/Vis/NIR spectrophotometer (LAMBDA 750, Perkin Elmer) with an integrating sphere. The thickness characterization was performed on a surface profiler (Alpha-Step IQ, KLA Tencor).

Photoelectrochemical measurements: The photoelectrochemical measurements were performed on a three-electrode configuration (PCI4/300™ potentiostat with the PHE200™ software, Gammy Electronic Instruments, Inc.). The glass supported photoanodes were tightly clamped to a stainless steel rod to serve as the working electrode, with a platinum foil and an Ag/AgCl as the counter and reference electrode respectively. Two aqueous electrolytes were employed for the PEC measurement, namely 0.5 M of Na_2SO_4 solution (PH 6) and 0.1 M KH_2PO_4 (KPi) buffer solution (PH 7, tuned by KOH). Electrical conductivity of the 0.1 M KPi solution was 12.5 mS cm^{-1}, as probed by an electrical conductivity meter. A 300 W Xe lamp (HAL-320, Asahi Spectra Co., Ltd) with AM 1.5G filter was used as the solar simulator, with 100 mW cm^{-2} light intensity irradiated at the center of working electrode. Photocurrent density was measured by linear sweep voltammetry (LSV) at a scan rate of 30 mV s^{-1}. For all cases, the light was irradiated on the front

side of FTO glass. Wherever not specified in the manuscript, the photoresponse data presented was measured using the smaller sized anode sample (1 cm × 2 cm). To study the effect of the illuminated area, homemade insulating resin masks with apertures of different sizes (4.02, 5.40, 8.00, 11.25, 15.86 mm in diameters) were used to hook on the illumination side of the PEC cell, regulating the incoming light irradiation to a fixed circular area (same as the aperture size) on the sample. These masks were only used on a 5 cm × 5 cm anode sample.

References:

[1] H. Zhang, W. Zhou, Y. Yang, C. Cheng, *Small* **2017**, *13*.
[2] S. J. A. Moniz, S. A. Shevlin, D. J. Martin, Z.-X. Guo, J. Tang, *Energy Environ. Sci.* **2015**, *8*, 731.
[3] I. D. Sharp, J. K. Cooper, F. M. Toma, R. Buonsanti, *ACS Energy Lett.* **2017**, *2*, 139.
[4] K. Sivula, R. van de Krol, *Nat. Rev. Mater.* **2016**, *1*, 15010.
[5] Z. Li, W. Luo, M. Zhang, J. Feng, Z. Zou, *Energy Environ. Sci.* **2013**, *6*, 347.
[6] B. Xie, H. Zhang, P. Cai, R. Qiu, Y. Xiong, *Chemosphere* **2006**, *63*, 956.
[7] C. Zachaus, F. F. Abdi, L. M. Peter, R. van de Krol, *Chem. Sci.* **2017**, *8*, 3712.
[8] Y. Park, K. J. McDonald, K. S. Choi, *Chem. Soc. Rev.* **2013**, *42*, 2321.
[9] D. K. Zhong, S. Choi, D. R. Gamelin, *J. Am. Chem. Soc.* **2011**, *133*, 18370.
[10] Y. Qiu, W. Liu, W. Chen, W. Chen, G. Zhou, P.-C. Hsu, R. Zhang, Z. Liang, S. Fan, Y. Zhang, Y. Cui, *Sci. Adv.* **2016**, *2*, e1501764.
[11] S. Sun, W. Wang, *RSC Adv.* **2014**, *4*, 47136.
[12] F. F. Abdi, L. Han, A. H. Smets, M. Zeman, B. Dam, R. van de Krol, *Nat. Commun.* **2013**, *4*, 2195.
[13] X. Chang, T. Wang, P. Zhang, J. Zhang, A. Li, J. Gong, *J. Am. Chem. Soc.* **2015**, *137*, 8356.
[14] K. J. McDonald, K.-S. Choi, *Energy Environ. Sci.* **2012**, *5*, 8553.
[15] Y. Kuang, Q. Jia, H. Nishiyama, T. Yamada, A. Kudo, K. Domen, *Adv. Energy Mater.* **2016**, *6*, 1501645.
[16] S. Hernández, G. Gerardi, K. Bejtka, A. Fina, N. Russo, *Appl. Catal., B* **2016**, *190*, 66.
[17] K. Tolod, S. Hernández, N. Russo, *Catalysts* **2017**, *7*, 13.
[18] J. A. Seabold, K. S. Choi, *J. Am. Chem. Soc.* **2012**, *134*, 2186.
[19] M. T. McDowell, M. F. Lichterman, J. M. Spurgeon, S. Hu, I. D. Sharp, B. S. Brunschwig, N. S. Lewis, *J. phys. Chem. C* **2014**, *118*, 19618.
[20] W. Luo, Z. Yang, Z. Li, J. Zhang, J. Liu, Z. Zhao, Z. Wang, S. Yan, T. Yu, Z. Zou, *Energy Environ. Sci.* **2011**, *4*, 4046.
[21] T. N. N. Parambath M. Sudeep, Aswathi Ganesan. Manikoth M. Shaijumon, Hyunseung Yang, Sehmus Ozden, Prabir K. Patra, Matteo Pasquali, Robert Vajtai, Sabyasachi Ganguli, Ajit K. Roy, Maliemadom R. Anantharaman, and Pulickel M. Ajayan, *ACS Nano* **2013**, *7*, 7034.
[22] X. Zhao, W. Luo, J. Feng, M. Li, Z. Li, T. Yu, Z. Zou, *Adv. Energy Mater.* **2014**, *4*, 1301785.

[23] L. Chen, F. M. Toma, J. K. Cooper, A. Lyon, Y. Lin, I. D. Sharp, J. W. Ager, *ChemSusChem* **2015**, *8*, 1066.
[24] H. S. Park, K. E. Kweon, H. Ye, E. Paek, G. S. Hwang, A. J. Bard, *J. phys. Chem. C* **2011**, *115*, 17870.
[25] H. Ye, H. S. Park, A. J. Bard, *J. Phys. Chem. C* **2011**, *115*, 12464.
[26] J. Jin, J. Yu, D. Guo, C. Cui, W. Ho, *Small* **2015**, *11*, 5262.
[27] J. K. Cooper, S. Gul, F. M. Toma, L. Chen, P.-A. Glans, J. Guo, J. W. Ager, J. Yano, I. D. Sharp, *Chem. Mater.* **2014**, *26*, 5365.
[28] J. Su, L. Guo, N. Bao, C. A. Grimes, *Nano Lett.* **2011**, *11*, 1928.
[29] C. Nguyen Van, T. H. Do, J. W. Chen, W. Y. Tzeng, K. A. Tsai, H. Song, H. J. Liu, Y. C. Lin, Y. C. Chen, C. L. Wu, C. W. Luo, W. C. Chou, R. Huang, Y. J. Hsu, Y. H. Chu, *NPG Asia Mater.* **2017**, *9*, e357.
[30] Y. Liang, T. Tsubota, L. P. A. Mooij, R. van de Krol, *J. Phys. Chem. C* **2011**, *115*, 17594.
[31] D. K. Zhong, J. Sun, H. Inumaru, D. R. Gamelin, *J. Am. Chem. Soc.* **2009**, *131*, 6086.
[32] D. K. Zhong, D. R. Gamelin, *J. Am. Chem. Soc.* **2009**, *132*, 4202.
[33] J. A. Seabold, K.-S. Choi, *Chem. Mater.* **2011**, *23*, 1105.
[34] F. F. Abdi, R. van de Krol, *J. Phys. Chem. C* **2012**, *116*, 9398.
[35] T. H. Jeon, W. Choi, H. Park, *Phys. Chem. Chem. Phys.* **2011**, *13*, 21392.
[36] S. Y. Chae, H. Jung, H. S. Jeon, B. K. Min, Y. J. Hwang, O.-S. Joo, *J. Mater. Chem. A* **2014**, *2*, 11408.
[37] H. W. Jeong, T. H. Jeon, J. S. Jang, W. Choi, H. Park, *J. Phys. Chem. C* **2013**, *117*, 9104.
[38] T. W. Kim, K. S. Choi, *Science* **2014**, *343*, 990.
[39] M. Dal Bó, V. Cantavella, E. Sánchez, D. Hotza, F. Gilabert, *J. Non Cryst. Solids.* **2013**, *363*, 70.
[40] X. Zhang, X. Quan, S. Chen, Y. Zhang, *J. Hazard. Mater.* **2010**, *177*, 914.
[41] F. M. Toma, J. K. Cooper, V. Kunzelmann, M. T. McDowell, J. Yu, D. M. Larson, N. J. Borys, C. Abelyan, J. W. Beeman, K. M. Yu, J. Yang, L. Chen, M. R. Shaner, J. Spurgeon, F. A. Houle, K. A. Persson, I. D. Sharp, *Nat. Commun.* **2016**, *7*, 12012.
[42] M. J. Kenney, M. Gong, Y. Li, J. Z. Wu, J. Feng, M. Lanza, H. Dai, *Science*, *342*, 836.
[43] Y. W. Chen, J. D. Prange, S. Duhnen, Y. Park, M. Gunji, C. E. Chidsey, P. C. McIntyre, *Nat. Mater.* **2011**, *10*, 539.
[44] J. Xie, C. Guo, P. Yang, X. Wang, D. Liu, C. M. Li, *Nano Energy* **2017**, *31*, 28.
[45] M. F. Lichterman, M. R. Shaner, S. G. Handler, B. S. Brunschwig, H. B. Gray, N. S. Lewis, J. M. Spurgeon, *J. Phys. Chem. Lett.* **2013**, *4*, 4188.
[46] A. Shinde, G. Li, L. Zhou, D. Guevarra, S. K. Suram, F. M. Toma, Q. Yan, J. A. Haber, J. B. Neaton, J. M. Gregoire, *J. Mater. Chem. A* **2016**, *4*, 14356.
[47] T. W. Kim, K. S. Choi, *J. Phys. Chem. Lett.* **2016**, *7*, 447.
[48] M. Zhong, T. Hisatomi, Y. Kuang, J. Zhao, M. Liu, A. Iwase, Q. Jia, H. Nishiyama, T. Minegishi, M. Nakabayashi, N. Shibata, R. Niishiro, C. Katayama, H. Shibano, M. Katayama, A. Kudo, T. Yamada, K. Domen, *J. Am. Chem. Soc.* **2015**, *137*, 5053.

Acknowledgements
Authors would like to thank National Research Foundation, Singapore for funding the CREATE program Singapore-Berkeley Research Initiative for Sustainable Energy (SinBeRISE) under which this project was done.